Finite Set Sensorless Control With Minimum a Priori Knowledge and Tuning Effort for Interior Permanent-Magnet Synchronous Motors

Anian Brosch, Fabio Tinazzi, *Member, IEEE*, Oliver Wallscheid, *Senior Member, IEEE*, Mauro Zigliotto, *Senior Member, IEEE*, and Joachim Böcker, *Senior Member, IEEE*

***Abstract*—By applying rotor angle sensorless control methods, the costs of the electrical drive can be decreased while its reliability is increased. Traditionally, the design of both the rotor angle estimator and the drive controller require a detailed motor model and manual tuning leading to significant effort by human experts. In this article, a rotor anisotropy-based sensorless control scheme for interior permanent-magnet synchronous motors is proposed that enables sensorless control with minimum tuning effort and a priori motor knowledge. Due to these characteristics, the scheme is particularly suitable for self-commissioning or low-cost drive applications. The scheme contains a finite control set model predictive current controller (FCS-MPCC) with an additional inequality constraint that enables the identification of the motor model in the stator-fixed coordinate system by using the last three measurement samples. Utilizing an automatic system identification procedure, the motor model is determined online in a data-driven fashion. The identified motor model serves both as prediction model of the FCS-MPCC and as baseline for the rotor angle estimation via an eigenvalue decomposition approach. Challenging experimental investigations at standstill up to the medium speed range prove the applicability of the proposed approach. Here, highly dynamic speed and current transients can be handled by the proposed method.**

***Index Terms*—Finite control set (FCS), identification, interior permanent magnet synchronous motor (IPMSM), low-speed operation, model predictive control, sensorless control, standstill.**

I. Introduction

ELECTRICAL drives are deployed in nearly every automated production line, in power plants, in various electrical devices, as well as in automotive applications. In many cases, interior permanent-magnet synchronous motors (IPMSM) are applied due to their high dynamics, efficiency, power, and torque density. By applying sensorless methods for the control of IPMSMs, the costs can be decreased while the reliability of the drive system is increased. Therefore, sensorless control is an important, ongoing research topic in academia and industry [1], [2].

A. State-of-the-Art Techniques

Sensorless control methods for IPMSMs can be classified into fundamental frequency-based methods for medium- and high-speed operation and rotor saliency-based methods for standstill and low-speed operation.

Fundamental frequency-based methods enable the observation of the rotor angle by incorporating the electromotive force (EMF) or the fundamental flux linkage with the help of a motor model of the electrical drive. The methods [3], [4], [5], and [6] are using both a rotor-angle-independent and a rotor-angle-dependent estimate of the EMF or flux linkage by incorporating model parameters, i.e., stator resistance, current-to-flux linkage look-up tables (LUT) or absolute inductances and permanent-magnet flux linkage. Here, the rotor angle is observed by adjusting its estimate in such a way that the rotor-angle-dependent estimate of the flux linkage or EMF is equal to the rotor-angle-independent estimate. Furthermore, the difference of predicted and measured current can be used to adjust angle and speed estimations with the help of classical feedback observers, e.g., extended Kalman filters [7], nonlinear Luenberger-inspired observers [8], and sliding-mode observers [9]. Since all fundamental frequency-based methods rely on the information that is provided via the EMF, a rotor angle estimation at or close to standstill fails because the EMF is too small. Therefore, these methods are not suitable for low-speed operation but only for medium- to high-speed operation.

Conversely, saliency-based methods are perfectly suited for standstill and low-speed operation. A necessary condition is a significant angle-dependent magnetic anisotropy of the rotor, which is identified with a high-frequency excitation voltage and the resulting response of the motor current. Here, sinusoidal voltages with frequency above the fundamental frequency are injected [10], [11], [12], [13]. With the help of filters, e.g., high- and low-pass filters [2] or least-squares (LS) estimators [13], the high-frequency currents and voltages are processed to estimate the rotor angle. Instead of sinusoidal voltages, rectangular-shaped voltage signals can be applied to identify the

Manuscript received 30 December 2022; revised 12 May 2023 and 22 June 2023; accepted 8 July 2023. Date of publication 12 July 2023; date of current version 1 September 2023. Recommended for publication by Associate Editor S. Kumar Mazumder. *(Corresponding author: Anian Brosch.)*

Anian Brosch, Oliver Wallscheid, and Joachim Böcker are with the Department of Power Electronics and Electrical Drives, Paderborn University, 33100 Paderborn, Germany (e-mail: anian.brosch@uni-paderborn.de; wallscheid@lea.upb.de; boecker@lea.upb.de).

Fabio Tinazzi and Mauro Zigliotto are with the Department of Management and Engineering, University of Padua, 36100 Vicenza, Italy (e-mail: fabio.tinazzi@unipd.it; mauro.zigliotto@unipd.it).

Color versions of one or more figures in this article are available at https://doi.org/10.1109/TPEL.2023.3294557.

Digital Object Identifier 10.1109/TPEL.2023.3294557

rotor anisotropy [14]. These rectangular signals can be injected additionally to the voltages of the drive controller [14], [15]. This approach is independent of the applied control scheme and can therefore be incorporated into, e.g., proportional-integral field-oriented control (PI-FOC), finite control set model predictive control (FCS-MPCC), etc. Alternatively, the voltage pulses produced by the applied control scheme in conjunction with the utilized inverter can be used for rotor angle estimation to allow drive operation without additional excitation [16], [17], [18], [19].

With the help of online identification schemes, the motor parameters for fundamental frequency-based and saliency-based methods can be adapted, and therefore, the control performance further increased [20], [21].

Although several of the referenced angle estimators do not require motor parameters to estimate the rotor angle, (e.g., [13]), a rough parameter estimate is usually necessary to setup the utilized control scheme, e.g., PI-FOC. Consequently, all previously mentioned methods require motor parameters, except the rotor anisotropy-based sensorless control schemes proposed in [11] and [17].

In [17], a recursive least-squares (RLS) estimator in the rotor-fixed dq coordinate system combined with a phase-locked loop (PLL) is proposed. With the help of the RLS and the inherently persistent current ripple excitation of the applied FCS-MPCC, the coefficients of the matrices of the discrete-time state-space representation of the motor in the dq coordinate system are identified. By utilizing a PLL, the rotor angle and speed are estimated. Although the simulative results seem promising, an experimental proof of the algorithm's effectiveness was not provided.

Similar to the formerly mentioned sensorless MPC scheme [17], the sensorless MPC scheme proposed in [11] is using an RLS estimator in the dq coordinate system for motor identification combined with a high-frequency signal injection method [10] for rotor angle estimation. However, the MPC method proposed in [11] is using a continuous-control-set (CCS) instead of an FCS. Due to the missing excitation of the CCS-MPCC during steady-state operation for regular sampling without additional current measurement, additional high-frequency signal injection is required for the motor model and rotor angle identification.

B. Contribution

In this article, a rotor saliency-based sensorless control scheme is proposed that does not require a priori motor parameters knowledge and need not be tuned. Due to these features, the scheme is ideally suited for self-commissioning and low-cost drive applications. Obviously, highest control performance in terms of either current distortion or control accuracy compared to fine-tuned sensorless control schemes that have full motor model information, e.g., differential inductance and flux linkage maps, cannot be expected. In addition to low-cost applications, the proposed approach can be used as part of an initial drive commissioning sequence followed by more accurate sensorloss control schemes, e.g., which require certain minimum speeds

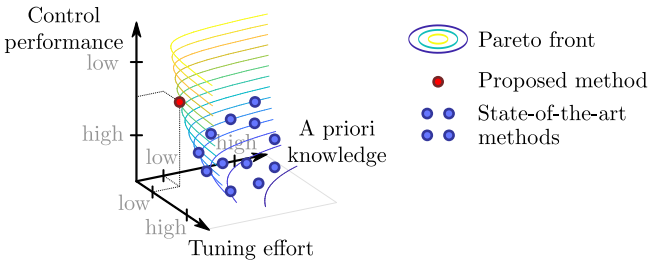

Fig. 1. Classification of the proposed method within a qualitative Pareto front of sensorless control methods regarding tuning effort of the control method, control performance, and a priori knowledge, e.g., motor parameters.

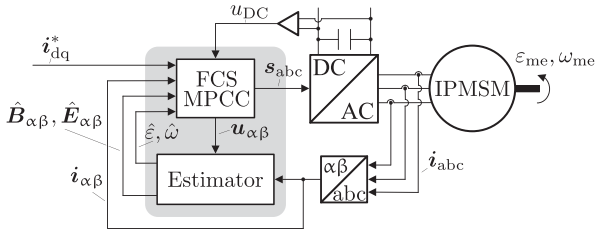

Fig. 2. Proposed sensorless control scheme that contains an FCS-MPCC and an estimation of the motor model, rotor angle, and speed (gray shaded part).

to allow evaluating the induced voltage information. Based on the authors' experience, a qualitative classification of the proposed method within a Pareto front of sensorless control methods regarding tuning effort, control performance, and a priori knowledge is shown in Fig. 1.

Compared to [11] and [17], which also do not require a priori motor parameter knowledge, the following advantages arise.

1) No additional harmonic signal injection with corresponding signal processing (demodulation, low-pass filtering, etc.) that is utilized in [11] is required.
2) The proposed technique does not require additional parameters to be tuned. Only for applications with highly dynamic speed transients, the characteristic frequency of a PLL should be adapted.

Furthermore, the applicability of the proposed method is experimentally proven under real-world conditions compared to the method investigated in [17], which was only evaluated based on idealized simulations.

The previously mentioned contributions are achieved by applying an FCS-MPCC with an additional inequality constraint to enable the identification of motor parameters and rotor angle; see Fig. 2. Herein, the last three state transitions are considered within a standard LS estimation procedure, which does not need a forgetting factor. On the basis of an admittance matrix $\boldsymbol{B}_{\alpha\beta}$ that is part of the identified motor model, an unfiltered rotor angle is extracted by solving an eigenvalue problem. To filter the identified rotor angle and to estimate the rotor speed, a standard PLL is applied.

C. Article Structure

The rest of this article is organized as follows. Section II describes the mathematical models of the inverter and IPMSM.

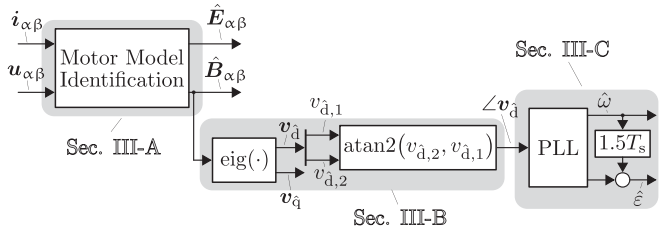

Fig. 3. Block diagram of the motor model, angle $\hat{\varepsilon}$, and speed estimation $\hat{\omega}$.

In Section III, the proposed sensorless control is presented. Extensive experimental steady-state and transient investigations of the proposed method are discussed in Section IV. Finally, Section V concludes this article.

II. Mathematical Model

In the following the mathematical models of the inverter and the IPMSM are provided within the rotor-fixed dq and the stator-fixed αβ reference frames. The motor model of the IPMSM in the αβ coordinate system represents the basis for identifying the motor model parameters and the rotor angle.

A. Coordinate Systems

A physical vector quantity $\boldsymbol{x}$ can be represented in the stator-fixed three-phase abc, in the stator-fixed αβ, or in the rotor-fixed dq coordinate system. Assuming a vanishing zero-sequence component $(x_\mathrm{a} + x_\mathrm{b} + x_\mathrm{c} = 0)$, the required transformations can be formulated as

$$\underbrace{\begin{bmatrix} x_\mathrm{d} \\ x_\mathrm{q} \end{bmatrix}}_{\boldsymbol{x}_\mathrm{dq}} = \underbrace{\begin{bmatrix} \cos(\varepsilon(t)) & \sin(\varepsilon(t)) \\ -\sin(\varepsilon(t)) & \cos(\varepsilon(t)) \end{bmatrix}}_{\boldsymbol{T}_{\mathrm{dq}\alpha\beta}(\varepsilon(t)) = \boldsymbol{T}^{-1}_{\alpha\beta\mathrm{dq}}(\varepsilon(t))} \overbrace{\frac{2}{3}\begin{bmatrix} 1 & -\frac{1}{2} & -\frac{1}{2} \\ 0 & \frac{\sqrt{3}}{2} & -\frac{\sqrt{3}}{2} \end{bmatrix}}^{\boldsymbol{T}_{\alpha\beta\mathrm{abc}}} \overbrace{\begin{bmatrix} x_\mathrm{a} \\ x_\mathrm{b} \\ x_\mathrm{c} \end{bmatrix}}^{\boldsymbol{x}_\mathrm{abc}}$$
$$\boldsymbol{x}_{\alpha\beta} = \begin{bmatrix} x_\alpha & x_\beta \end{bmatrix}^\intercal \tag{1}$$

wherein ε denotes the electrical rotor angle of the PMSM.

B. Voltage Inverter Equations

The finite number of possible switching states are translated to a finite set of voltages in the αβ frame. For a three-phase, two-level inverter, these voltages are given by

$$\boldsymbol{u}_{\alpha\beta} \in \left\{ \boldsymbol{u}_{\alpha\beta} \in \mathbb{R}^2 | \boldsymbol{u}_{\alpha\beta} = u_{DC} \boldsymbol{T}_{\alpha\beta\mathrm{abc}} \boldsymbol{s}_\mathrm{abc} \right\} \tag{2}$$

with u_DC as the dc-link voltage and $\boldsymbol{s}_\mathrm{abc}$ as the switching state of the inverter defined by

$$\boldsymbol{s}_\mathrm{abc} = \begin{bmatrix} s_\mathrm{a} & s_\mathrm{b} & s_\mathrm{c} \end{bmatrix}^\intercal \in \{0,1\}^3 . \tag{3}$$

With the aforementioned equations, the stator voltage $\boldsymbol{u}_\mathrm{dq}$ is given by

$$\boldsymbol{u}_\mathrm{dq} = \boldsymbol{T}_{\mathrm{dq}\alpha\beta}(\varepsilon) \boldsymbol{u}_{\alpha\beta} = u_\mathrm{DC} \boldsymbol{T}_{\mathrm{dqabc}}(\varepsilon) \boldsymbol{s}_\mathrm{abc}. \tag{4}$$

C. Discrete-Time IPMSM White-Box Model

The discrete-time current difference equation of an IPMSM considering (cross-)saturation effects in the dq coordinate system can be described as follows [22]:

$$\begin{aligned} \boldsymbol{i}_\mathrm{dq}[k+1] &= \boldsymbol{i}_\mathrm{dq}[k] + \boldsymbol{B}_\mathrm{dq}(\boldsymbol{i}_\mathrm{dq}[k], \omega[k]) \boldsymbol{u}_\mathrm{dq}[k] \\ &\quad + \boldsymbol{E}_\mathrm{dq}(\boldsymbol{i}_\mathrm{dq}[k], \omega[k]) \end{aligned}$$

with:

$$\begin{aligned} \boldsymbol{B}_\mathrm{dq}(\boldsymbol{i}_\mathrm{dq}[k], \omega[k]) &= \boldsymbol{L}^{-1}_{\mathrm{dq},\Delta}(\boldsymbol{i}_\mathrm{dq}[k]) \boldsymbol{T}_{\alpha\beta\mathrm{dq}}(-T_\mathrm{s}\omega[k]) T_\mathrm{s} \\ \boldsymbol{E}_\mathrm{dq}(\boldsymbol{i}_\mathrm{dq}[k], \omega[k]) &= \boldsymbol{L}^{-1}_{\mathrm{dq},\Delta}(\boldsymbol{i}_\mathrm{dq}[k]) \\ &\quad \cdot \Big[\left[\boldsymbol{T}_{\alpha\beta\mathrm{dq}}(-T_\mathrm{s}\omega[k]) - \boldsymbol{I} \right] \boldsymbol{\psi}_\mathrm{dq}(\boldsymbol{i}_\mathrm{dq}[k]) \\ &\quad - R_\mathrm{s} T_\mathrm{s} \boldsymbol{i}_\mathrm{dq}[k] \Big]. \end{aligned} \tag{5}$$

Here, $\boldsymbol{i}_\mathrm{dq}$ represents the stator current, $\boldsymbol{\psi}_\mathrm{dq}(\boldsymbol{i}_\mathrm{dq})$ the flux linkage, $\boldsymbol{u}_\mathrm{dq}$ the stator voltage, ω the electrical angular velocity, R_s the ohmic stator resistance, T_s the sampling time, $\boldsymbol{I}$ the identity matrix, and $\boldsymbol{L}_{\mathrm{dq},\Delta}$ the differential inductance matrix, which is defined by

$$\boldsymbol{L}_{\mathrm{dq},\Delta}(\boldsymbol{i}_\mathrm{dq}) = \begin{bmatrix} L_\mathrm{dd}(\boldsymbol{i}_\mathrm{dq}) & L_\mathrm{dq}(\boldsymbol{i}_\mathrm{dq}) \\ L_\mathrm{qd}(\boldsymbol{i}_\mathrm{dq}) & L_\mathrm{qq}(\boldsymbol{i}_\mathrm{dq}) \end{bmatrix} = \begin{bmatrix} \frac{\partial \psi_\mathrm{d}}{\partial i_\mathrm{d}} & \frac{\partial \psi_\mathrm{d}}{\partial i_\mathrm{q}} \\ \frac{\partial \psi_\mathrm{q}}{\partial i_\mathrm{d}} & \frac{\partial \psi_\mathrm{q}}{\partial i_\mathrm{q}} \end{bmatrix}. \tag{6}$$

The term $\boldsymbol{T}_{\alpha\beta\mathrm{dq}}(-T_\mathrm{s}\omega)$ in (5) considers the rotation of the dq against the αβ coordinate system during one sampling period [23], [24]. For compactness, the parameter-varying matrices $\boldsymbol{B}_\mathrm{dq}(\boldsymbol{i}_\mathrm{dq}[k], \omega[k])$, $\boldsymbol{E}_\mathrm{dq}(\boldsymbol{i}_\mathrm{dq}[k], \omega[k])$ are abbreviated with $\boldsymbol{B}_\mathrm{dq}[k]$, $\boldsymbol{E}_\mathrm{dq}[k]$ in the following.

By applying coordinate transformations (1), the IPMSM motor model in the dq coordinates can be transformed to the αβ coordinate system

$$\begin{aligned} \boldsymbol{i}_{\alpha\beta}[k+1] &= \boldsymbol{i}_{\alpha\beta}[k] + \boldsymbol{B}_{\alpha\beta}[k] \boldsymbol{u}_{\alpha\beta}[k] + \boldsymbol{E}_{\alpha\beta}[k] \\ &\text{with} \\ \boldsymbol{B}_{\alpha\beta}[k] &= \boldsymbol{T}_{\alpha\beta\mathrm{dq}}(\varepsilon[k+1]) \boldsymbol{B}_\mathrm{dq}[k] \boldsymbol{T}_{\mathrm{dq}\alpha\beta}(\varepsilon[k]) \\ &= \begin{bmatrix} b_{11}[k] & b_{12}[k] \\ b_{21}[k] & b_{22}[k] \end{bmatrix} \\ \boldsymbol{E}_{\alpha\beta}[k] &= \boldsymbol{T}_{\alpha\beta\mathrm{dq}}(\varepsilon[k+1]) \boldsymbol{E}_\mathrm{dq}[k] \\ &\quad + \left[\boldsymbol{T}_{\alpha\beta\mathrm{dq}}(T_\mathrm{s}\omega[k]) - \boldsymbol{I} \right] \boldsymbol{i}_{\alpha\beta}[k] = \begin{bmatrix} e_1[k] \\ e_2[k] \end{bmatrix}. \end{aligned} \tag{7}$$

Here, the term $[\boldsymbol{T}_{\alpha\beta\mathrm{dq}}(T_\mathrm{s}\omega) - \boldsymbol{I}]\boldsymbol{i}_{\alpha\beta}$ in $\boldsymbol{E}_{\alpha\beta}$ considers the rotation of the current $\boldsymbol{i}$ in the dq against the αβ frame.

III. Sensorless Control

In this section, the proposed rotor saliency-based sensorless current control without the knowledge of any motor parameters is presented. This makes the scheme particular interesting for automated (low-cost) drive commissioning procedures as it does not require any prior human work contribution. The sensorless

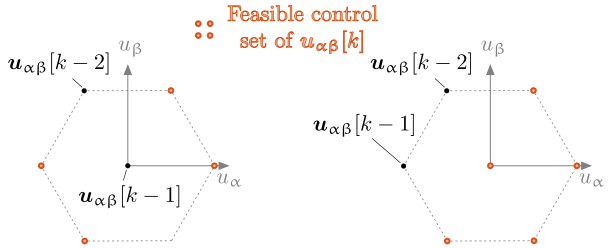

Fig. 4. Two exemplary feasible control sets for the input voltage $\boldsymbol{u}_{\alpha\beta}[k]$ to ensure a nonsingular regressor matrix $\boldsymbol{\Xi}$.

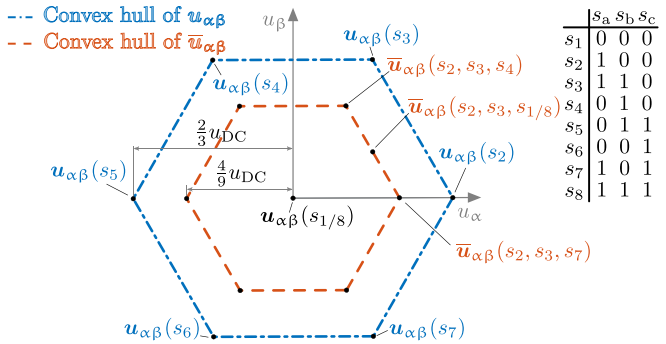

Fig. 5. Convex hulls of the elementary vectors $\boldsymbol{u}_{\alpha\beta}$ and the mean voltages $\overline{\boldsymbol{u}}_{\alpha\beta}$ (12) by applying the inequality condition (11).

control contains an estimation of the motor model, rotor angle, and rotor speed as well as an FCS-MPCC. A block diagram outlining the motor model identification, angle and speed estimation is shown in Fig. 3.

A. Motor Model Identification

Instead of estimating the motor model in the dq frame, identification is performed in αβ coordinates. In this way, no feedback paths from the estimated angle $\hat{\varepsilon}$ for rotor transformations are required in the position estimation algorithm. These feedback paths would lead to additional time delays due to the low-pass filter characteristic of the PLL, which would negatively affect the achievable dynamics and stability of the overall sensorless control.

The matrices $\boldsymbol{B}_{\mathrm{dq}}$ and $\boldsymbol{E}_{\mathrm{dq}}$ that describe the dynamics of $\boldsymbol{i}_{\mathrm{dq}}$ are constant for steady-state operation points defined by $\boldsymbol{i}_{\mathrm{dq}}$ and ω. However, in the αβ coordinate system, the corresponding matrices $\boldsymbol{B}_{\alpha\beta}$ and $\boldsymbol{E}_{\alpha\beta}$ are a function of the rotor angle ε, even for constant $\boldsymbol{i}_{\mathrm{dq}}$ and ω. In order to prevent a large variation of the rotor angle ε in the data that is used for the motor model identification, $\boldsymbol{B}_{\alpha\beta}$ and $\boldsymbol{E}_{\alpha\beta}$ must be identified with the lowest feasible number of consecutive state transitions. This is achieved by rearranging the motor model (7) and identifying the entries of $\boldsymbol{B}_{\alpha\beta}$ and $\boldsymbol{E}_{\alpha\beta}$ with two separate LS problems, one for each of the α- and β-axes

$$\underbrace{\begin{bmatrix} i_\alpha[k]-i_\alpha[k-1] \\ i_\alpha[k-1]-i_\alpha[k-2] \\ i_\alpha[k-2]-i_\alpha[k-3] \end{bmatrix}}_{\boldsymbol{\Gamma}_\alpha[k]} = \underbrace{\begin{bmatrix} u_\alpha[k-1] & u_\beta[k-1] & 1 \\ u_\alpha[k-2] & u_\beta[k-2] & 1 \\ u_\alpha[k-3] & u_\beta[k-3] & 1 \end{bmatrix}}_{\boldsymbol{\Xi}[k]} \underbrace{\begin{bmatrix} b_{11} \\ b_{12} \\ e_1 \end{bmatrix}}_{\hat{\boldsymbol{\theta}}_\alpha[k]} \tag{8}$$

$$\underbrace{\begin{bmatrix} i_\beta[k]-i_\beta[k-1] \\ i_\beta[k-1]-i_\beta[k-2] \\ i_\beta[k-2]-i_\beta[k-3] \end{bmatrix}}_{\boldsymbol{\Gamma}_\beta[k]} = \boldsymbol{\Xi}[k] \underbrace{\begin{bmatrix} b_{21} \\ b_{22} \\ e_2 \end{bmatrix}}_{\hat{\boldsymbol{\theta}}_\beta[k]} \tag{9}$$

with the measurement vectors $\boldsymbol{\Gamma}_{\alpha/\beta}$, the regressor matrix $\boldsymbol{\Xi}$, and the parameter vectors $\hat{\boldsymbol{\theta}}_{\alpha/\beta}$. The entries of $\boldsymbol{B}_{\alpha\beta}$ and $\boldsymbol{E}_{\alpha\beta}$ can be calculated by solving (8) and (9) for $\hat{\boldsymbol{\theta}}_{\alpha/\beta}$

$$\hat{\boldsymbol{\theta}}_{\alpha/\beta}[k] = (\boldsymbol{\Xi}[k])^{-1}\boldsymbol{\Gamma}_{\alpha/\beta}[k]. \tag{10}$$

To ensure an invertible regressor matrix $\boldsymbol{\Xi}$, the last three applied voltages $\boldsymbol{u}_{\alpha\beta}$ must not lie on a straight line in the αβ coordinate system. This constraint is formulated as an inequality condition that must be satisfied by the FCS-MPCC

$$\boldsymbol{0} \neq (\boldsymbol{u}_{\alpha\beta}[k-2]-\boldsymbol{u}_{\alpha\beta}[k-1]) \times (\boldsymbol{u}_{\alpha\beta}[k-1]-\boldsymbol{u}_{\alpha\beta}[k]). \tag{11}$$

A graphical representation of the remaining feasible control actions $\boldsymbol{u}_{\alpha\beta}[k]$ for given exemplary past voltages $\boldsymbol{u}_{\alpha\beta}[k-1]$, $\boldsymbol{u}_{\alpha\beta}[k-2]$ is depicted in Fig. 4. With regard to the identification of the motor model, the inequality condition (11) is advantageous, since it provides additional excitation that is required such that three state transitions are sufficient for the identification.

However, this constraint also leads to two disadvantages. First, some possible optimal control actions with respect to the FCS-MPCC cost function (24a) cannot be chosen due to the inequality condition (11). Instead, suboptimal voltage vectors must be chosen. This leads to an increased distortion of the phase currents, as investigated experimentally in Section IV. Second, the available average voltage is decreased by a factor of 1/3. The reason can be analyzed by averaging the allowed voltage vectors over the last three sampling instants

$$\overline{\boldsymbol{u}}_{\alpha\beta}(\boldsymbol{s}_{\mathrm{abc}}[k],\boldsymbol{s}_{\mathrm{abc}}[k-1],\boldsymbol{s}_{\mathrm{abc}}[k-2]) = \frac{\sum_{i=0}^{2}\boldsymbol{u}_{\alpha\beta}(\boldsymbol{s}_{\mathrm{abc}}[k-i])}{3}. \tag{12}$$

In Fig. 5, the convex hull of the elementary voltage vectors $\boldsymbol{u}_{\alpha\beta}$, which corresponds to the voltage hexagon as well as the convex hull of possible mean voltages $\overline{\boldsymbol{u}}_{\alpha\beta}$ defined in (12) by applying the inequality condition (11) are depicted. The latter corresponds to the voltage hexagon with a reduction of size by a factor of 1/3. Due to the effect of the reduced applicable average voltages, the proposed sensorless control is not suited for high-speed operation in the constant power region at the voltage limit.

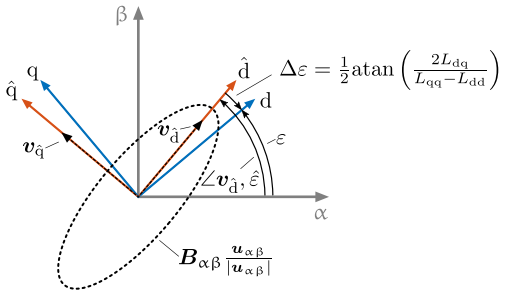

Fig. 6. Graphical illustration of the rotor angle estimation by solving an eigenvalue problem and the resulting systematic estimation error $\Delta\varepsilon$ due to neglected cross-saturation effects.

B. Rotor Angle Estimation

The rotor angle is estimated via the angle-dependent magnetic reluctance of IPMSM rotors. This rotor anisotropy information is contained in the identified matrix $\hat{\boldsymbol{B}}_{\alpha\beta}$. Here, $\hat{\boldsymbol{B}}_{\alpha\beta}$ can be interpreted as the admittance matrix for the harmonic content of currents $\boldsymbol{i}_{\alpha\beta}$ and voltages $\boldsymbol{u}_{\alpha\beta}$. For IPMSMs without cross-saturation effects, the direction in which most amplification applies to normalized voltage excitation corresponds to the d-axis and the direction in which it is amplified the least corresponds to the q-axis since $L_{\text{dd}} < L_{\text{qq}}$; cf., Fig. 6. Therefore, the rotor angle can be estimated by solving the following eigenvalue problem:

$$\hat{\boldsymbol{B}}_{\alpha\beta}[k]\boldsymbol{v}_{\hat{\text{d}}/\hat{\text{q}}}[k] = \lambda_{\hat{\text{d}}/\hat{\text{q}}}[k]\boldsymbol{v}_{\hat{\text{d}}/\hat{\text{q}}}[k]. \tag{13}$$

Due to $L_{\text{dd}} < L_{\text{qq}}$, resulting current amplitudes for unit voltage excitations are amplified the most in the d-axis direction, and therefore, the eigenvector $\boldsymbol{v}_{\hat{\text{d}}/\hat{\text{q}}}$ with the greater eigenvalue $\lambda_{\hat{\text{d}}}$ corresponds to the d-axis direction. The angle $\angle\boldsymbol{v}_{\hat{\text{d}}}$ of the eigenvector $\boldsymbol{v}_{\hat{\text{d}}}$ that is aligned with the d-axis is calculated by

$$\angle\boldsymbol{v}_{\hat{\text{d}}}[k] = \text{atan2}\left(v_{\hat{\text{d}},2}[k], v_{\hat{\text{d}},1}[k]\right) \tag{14}$$

and can be interpreted as an unfiltered estimate of the rotor angle ε. Here, the function atan2 is the two-argument arctangent that returns angle values from the interval $[-\pi, \pi]$. Moreover, to reduce the high-frequency noise content of the rotor angle estimate $\angle\boldsymbol{v}_{\hat{\text{d}}}$, a standard PLL is applied that is described in Section III-C. The high-frequency content of $\angle\boldsymbol{v}_{\hat{\text{d}}}$ is mainly induced by parasitic effects, e.g., measurement noise and position-dependent estimation errors due to a nonsinusoidal flux distribution in the air gap. The filtered rotor angle estimate of the PLL is denoted as $\hat{\varepsilon}$ and the rotor angle estimation error is defined as

$$\Delta\varepsilon = \varepsilon - \hat{\varepsilon}. \tag{15}$$

Here, a portion

$$\Delta\varepsilon_{\text{cross}} = \frac{1}{2}\text{atan}\left(\frac{2L_{\text{dq}}(\boldsymbol{i}_{\text{dq}})}{L_{\text{qq}}(\boldsymbol{i}_{\text{dq}}) - L_{\text{dd}}(\boldsymbol{i}_{\text{dq}})}\right) \tag{16}$$

of the estimation error $\Delta\varepsilon$ is introduced by cross-saturation effects [25]. For model-based schemes with the knowledge of the magnetization (differential inductances LUTs), this systematic error can be easily compensated by adding the right-hand side of (16) to the rotor angle estimate $\hat{\varepsilon}$. Instead, for the proposed scheme, the information of the cross saturation is not available, and therefore, the systematic estimation error (16) is inevitable [26].

In general, rotor anisotropy-based schemes are not able to identify the correct polarity (sign) of the d- and q-axes. Either an angle $\hat{\varepsilon}$ that is inline with the actual rotor angle ε (or slightly shifted due to systematic estimation errors) or a rotor angle $\hat{\varepsilon}$ that points into the opposite direction, since it is shifted by an angle of π, is estimated. This shift must be prevented for the sensorless control of IPMSMs.

To determine the polarity of the d- and q-axes, two short voltage pulses in both directions of the d-axis can be injected since a certain current magnitude is reached with the sensorless control at the startup of the drive system. The current transient that requires less voltage over time is in deeper saturation, and therefore, aligned with the d-axis due to the permanent-magnet flux [27].

In order to prevent the estimated angle $\hat{\varepsilon}$ from shifting by π during online operation, the following condition is applied:

if $|\text{mod}\left(\hat{\varepsilon}[k-1] - \angle\boldsymbol{v}_{\hat{\text{d}}}[k] + \pi, 2\pi\right) - \pi| > \frac{\pi}{2}$ then

$\angle\boldsymbol{v}_{\hat{\text{d}}}[k] \leftarrow \angle\boldsymbol{v}_{\hat{\text{d}}}[k] + \pi$

end if.

Here, the momentary unfiltered rotor angle estimate $\angle\boldsymbol{v}_{\hat{\text{d}}}[k]$ is compared to the filtered rotor angle estimate $\hat{\varepsilon}[k-1]$ of the previous time step. If the absolute value of the difference of $\angle\boldsymbol{v}_{\hat{\text{d}}}[k]$ and $\hat{\varepsilon}[k-1]$, mapped to the interval $[-\pi, \pi]$ with the help of the modulo function, is greater than $\pi/2$, the unfiltered rotor angle estimate $\angle\boldsymbol{v}_{\hat{\text{d}}}[k]$ was shifted by an angle of π. This shift can occur during the solution of the eigenvalue problem, since the polarity of the dq reference frame cannot be determined. To stay with the correct polarity that is determined at the startup of the drive, these shifts must be compensated. This is achieved by shifting $\angle\boldsymbol{v}_{\hat{\text{d}}}[k]$ additionally with an angle of π.

C. Phase-Locked Loop (PLL)

As mentioned previously, a standard PLL is applied to reduce the high-frequency noise content of the estimated rotor angle. Additionally, the PLL provides a smoothed estimate of the rotor speed $\hat{\omega}$.

Assuming $\angle\boldsymbol{v}_{\hat{\text{d}}}$ and $\hat{\varepsilon}$ are available in continuous time, the PLL operation can be described by means of a transfer function with the Laplace transform variable ξ. Furthermore, for the analysis of the PLL, it is assumed that the angles $\angle\boldsymbol{v}_{\hat{\text{d}}}$ and $\hat{\varepsilon}$ are not restricted to the interval $[-\pi, \pi]$ by modulo functions or the arctangent in (14) but are continuously continued without restriction so that step-like changes are avoided. A block diagram of the PLL with the damping D and the characteristic frequency ω_0 as tuning parameters that define the proportional and integral gains of the PI controller is depicted in Fig. 7. In the actual implementation of the PLL, however, modulo functions are included that are omitted in the simplified diagram of Fig. 7.

The portion of the angle estimation error that is introduced by the PLL during transient processes is denoted as

$$\Delta\varepsilon_{\text{PLL}} = \angle\boldsymbol{v}_{\hat{\text{d}}} - \hat{\varepsilon}. \tag{17}$$

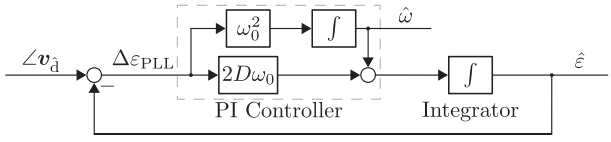

Fig. 7. Simplified block diagram of the applied PLL.

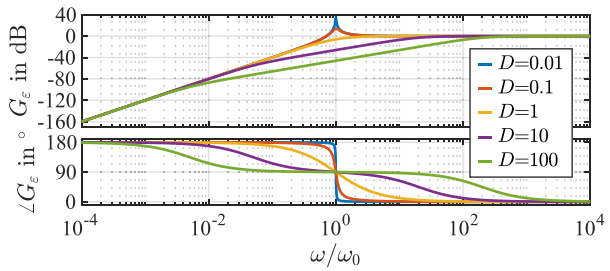

Fig. 8. Bode plot of the transfer function $G_\varepsilon(\xi)$ from input $\angle \boldsymbol{v}_{\hat{\mathrm{d}}}(\xi)$ to output $\angle \boldsymbol{v}_{\hat{\mathrm{d}}}(\xi) - \hat{\varepsilon}(\xi)$.

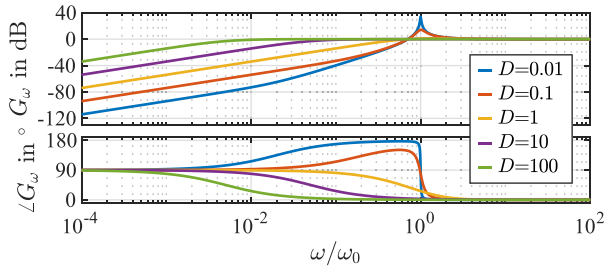

Fig. 9. Bode plot of the transfer function $G_\omega(\xi)$ from input $\omega(\xi)$ to output $\omega(\xi) - \hat{\omega}(\xi)$.

The transfer function from the unfiltered rotor angle estimate $\angle \boldsymbol{v}_{\hat{\mathrm{d}}}(\xi)$ to the rotor angle observation error $\Delta\varepsilon_{\mathrm{PLL}}(\xi)$ induced by the PLL evaluates to

$$G_\varepsilon(\xi) = \frac{\Delta\varepsilon_{\mathrm{PLL}}(\xi)}{\angle \boldsymbol{v}_{\hat{\mathrm{d}}}(\xi)} = \frac{\frac{1}{\omega_0^2}}{\frac{1}{\omega_0^2}\xi^2 + 2\frac{D}{\omega_0}\xi + 1}. \tag{18}$$

For the following analysis of the PLL, it is assumed that $\omega(\xi) = \xi \angle \boldsymbol{v}_{\hat{\mathrm{d}}}(\xi)$ holds. Hence, the transfer function of the rotor speed $\omega(\xi)$ to the rotor speed observation error $\Delta\omega_{\mathrm{PLL}} = \omega(\xi) - \hat{\omega}(\xi)$ results in

$$G_\omega(\xi) = \frac{\Delta\omega_{\mathrm{PLL}}(\xi)}{\omega(\xi)} = \frac{\frac{1}{\omega_0^2}\xi^2 + 2\frac{D}{\omega_0}\xi}{\frac{1}{\omega_0^2}\xi^2 + 2\frac{D}{\omega_0}\xi + 1}. \tag{19}$$

Both transfer functions (18) and (19) are shown in Figs. 8 and 9 for different damping ratios D. In order to ensure a suppression of the rotor angle and speed observation errors up to ω_0 without amplifications of the observation errors near ω_0, a damping ratio of $D = 1$ is recommended; cf., Figs. 8 and 9.

A tradeoff between fast estimation dynamics and satisfactory noise suppression must be found by selecting ω_0. A procedure to calculate a suitable characteristic frequency is described in the following.

The transfer function from the rotor acceleration $a(\xi) = \xi\omega(\xi)$ to the rotor angle observation error of the PLL is given by

$$G_a(\xi) = \frac{\Delta\varepsilon_{\mathrm{PLL}}(\xi)}{a(\xi)} = \frac{\frac{1}{\omega_0^2}}{\frac{1}{\omega_0^2}\xi^2 + 2\frac{D}{\omega_0}\xi + 1}. \tag{20}$$

With the help of this transfer function, the steady-state angle estimation error of the PLL during speed ramps ($\xi = 0$) with the slope a for a given characteristic frequency can be calculated

$$\Delta\varepsilon_{\mathrm{PLL}} = \frac{a}{\omega_0^2}. \tag{21}$$

The aforementioned equation yields the minimum required characteristic frequency in order not to exceed a max error $\Delta\varepsilon_{\mathrm{PLL,max}}$ at an acceleration $a_{\max}$ as follows:

$$\omega_0 = \sqrt{\frac{a_{\max}}{\Delta\varepsilon_{\mathrm{PLL,max}}}}. \tag{22}$$

Here, a characteristic frequency of $\omega_0 = 2\pi \cdot 50\,\mathrm{Hz}$ represents a suitable compromise between fast estimation dynamics and satisfactory noise suppression. Therefore, $D = 1$ and $\omega_0 = 2\pi \cdot 50\,\mathrm{Hz}$ are chosen for the remainder of this article. In addition, it can be assumed that this parametrization is useful for the majority of sensorless drive applications (especially in the area of low-cost drives or for initial commissioning), and can therefore, be stored as a constant configuration in the control software. Manual retuning of the characteristic frequency ω_0 is only necessary for applications with highly dynamic speed changes. Here, ω_0 can be adapted using (22) for specified speed ramps and angle observation error.

For the digital implementation of the PLL, however, it must be considered that $\angle \boldsymbol{v}_{\hat{\mathrm{d}}}[k]$, $\hat{\varepsilon}[k]$, and $\hat{\omega}[k]$ are sampled signals, and therefore, also the PLL must be implemented in a discrete-time fashion, e.g., by mapping the block diagram of the PLL in Fig. 7 to its discrete-time equivalent.

Since the rotor angle is estimated within the last three state transitions, an additional prerotation by 1.5 sampling periods T_s of the estimated rotor angle must be conducted (see Fig. 3)

$$\hat{\varepsilon}[k] \leftarrow \hat{\varepsilon}[k] + 1.5T_\mathrm{s}\hat{\omega}[k]. \tag{23}$$

D. Finite-Control-Set Model Predictive Current Control (FCS-MPCC)

An established FCS-MPCC is applied to steer the current in the estimated dq frame $\boldsymbol{i}_{\hat{\mathrm{dq}}}$ to its reference $\boldsymbol{i}^*_{\mathrm{dq}}$ as

$$\min_{\boldsymbol{s}_{\mathrm{abc}}[k]} \quad \|\boldsymbol{i}^*_{\mathrm{dq}}[k+1] - \boldsymbol{i}_{\hat{\mathrm{dq}}}[k+1]\|_2^2 \tag{24a}$$

$$\text{s.t.} \quad \boldsymbol{u}_{\alpha\beta}[k] = u_{\mathrm{DC}}\boldsymbol{T}_{\alpha\beta\mathrm{abc}}\boldsymbol{s}_{\mathrm{abc}}[k] \tag{24b}$$

$$\boldsymbol{u}_{\hat{\mathrm{dq}}}[k] = \boldsymbol{T}_{\mathrm{dq}\alpha\beta}(\hat{\varepsilon}[k])\boldsymbol{u}_{\alpha\beta}[k] \tag{24c}$$

$$\boldsymbol{0} \neq (\boldsymbol{u}_{\alpha\beta}[k-2] - \boldsymbol{u}_{\alpha\beta}[k-1]) \times (\boldsymbol{u}_{\alpha\beta}[k-1] - \boldsymbol{u}_{\alpha\beta}[k]) \tag{24d}$$

$$\boldsymbol{i}_{\hat{\mathrm{dq}}}[k+1] = \boldsymbol{i}_{\hat{\mathrm{dq}}}[k] + \hat{\boldsymbol{B}}_{\hat{\mathrm{dq}}}[k]\boldsymbol{u}_{\hat{\mathrm{dq}}}[k] + \hat{\boldsymbol{E}}_{\hat{\mathrm{dq}}}[k]. \tag{24e}$$

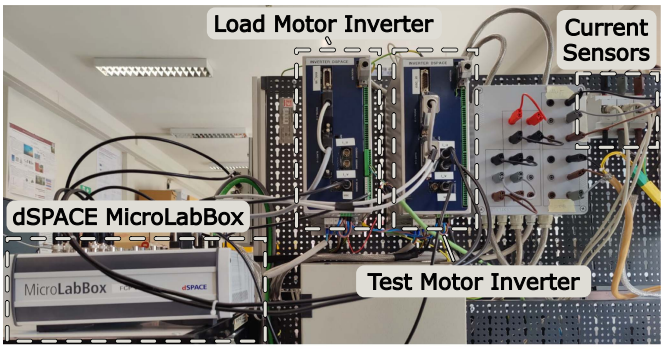

(a)

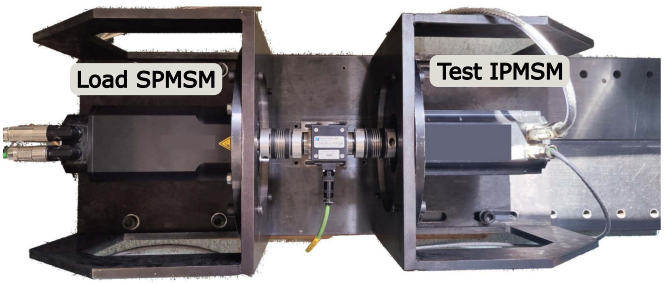

(b)

Fig. 10. Test bench. (a) Power electronic devices and dSPACE rapid-control-prototyping system. (b) Load motor and test IPMSM.

Here, the required estimated system matrices $\hat{\boldsymbol{B}}_{\mathrm{d\hat{q}}}$ and $\hat{\boldsymbol{E}}_{\mathrm{d\hat{q}}}$ in the estimated dq frame are given by

$$\hat{\boldsymbol{B}}_{\mathrm{d\hat{q}}}[k] = \boldsymbol{T}_{\mathrm{dq}\alpha\beta}(\hat{\varepsilon}[k+1])\hat{\boldsymbol{B}}_{\alpha\beta}[k]\boldsymbol{T}_{\alpha\beta\mathrm{dq}}(\hat{\varepsilon}[k]) \tag{25}$$

$$\hat{\boldsymbol{E}}_{\mathrm{d\hat{q}}}[k] = \boldsymbol{T}_{\mathrm{dq}\alpha\beta}(\hat{\varepsilon}[k+1]) \cdot \left[\hat{\boldsymbol{E}}_{\alpha\beta}[k] - [\boldsymbol{T}_{\alpha\beta\mathrm{dq}}(T_\mathrm{s}\hat{\omega}[k]) - \boldsymbol{I}]\, \boldsymbol{i}_{\alpha\beta}[k]\right] \tag{26}$$

with $\hat{\boldsymbol{B}}_{\alpha\beta}$ and $\hat{\boldsymbol{E}}_{\alpha\beta}$ estimated by the motor model identification described in Section III-A and $\hat{\varepsilon}[k+1]$ approximated via $\hat{\varepsilon}[k] + T_\mathrm{s}\hat{\omega}[k]$; cf., (7).

Instead (24), any FCS-related control approach can be combined with the proposed sensorless control as long as the inequality condition (24d) is satisfied. To compensate for the control delay of one sampling period induced by the digital implementation, a one-step prediction as in [28] is applied. Furthermore, the current prediction error arising from the inverter interlocking time to prevent hard short circuits in each inverter half bridge is compensated [29].

IV. Experimental Investigation

A. Test Setup

All following experimental results have been obtained on a laboratory test bench, which is depicted in Fig. 10. The electrical drive system under test consists of an IPMSM for industrial applications with a two-level IGBT inverter. The datasheet parameters of the test motor are provided in Table I. Flux linkage maps $\boldsymbol{\psi}_{\mathrm{dq}}(\boldsymbol{i}_{\mathrm{dq}})$ of the test motor were obtained via an offline, fundamental frequency-based characterization scheme [30], and are depicted in Fig. 11. The corresponding differential inductances $\boldsymbol{L}_{\mathrm{dq}}(\boldsymbol{i}_{\mathrm{dq}})$ are calculated by partially differentiating the flux linkage maps [cf., (6)] and can be seen in Fig. 12. As load motor, a speed-controlled SPMSM is mechanically coupled with the test motor. Furthermore, the test bench is equipped with a dSPACE MicroLabBox rapid-control-prototyping system. All measurements have been obtained by the dSPACE analog–digital converters, which have been synchronized with the control task. The sensorless control and most important inverter parameters are listed in Table I. In Table II, the required execution time of the proposed sensorless control scheme, implemented in C running on a Lenovo T14 s with an AMD Ryzen 7 1.9 GHz processor and 32 GB of RAM, is listed. It is worth to note that only one processor core was used. Since the execution time of motor model

TABLE I
IPMSM, Inverter, and Control Parameters

IPMSM		
Nominal speed	$n_{\mathrm{me,nom}}$	$3000\,\mathrm{min}^{-1}$
Nominal torque	T_nom	$7\,\mathrm{Nm}$
Nominal current	I_nom	$4.2\,\mathrm{A}$
Pole pair number	p	2
Stator resistance	R_s	$2.7\,\Omega$
Permanent magnet flux	ψ_p	$0.22\,\mathrm{Vs}$
Inductances	L_d	$0.02\,\mathrm{H}$
	L_q	$0.11\,\mathrm{H}$
Inverter		
Typology		Voltage source inverter 2-level, IGBT
DC-link voltage	u_DC	$540\,\mathrm{V}$
Inverter interlocking time	T_i	$2\,\mu\mathrm{s}$
Sensorless control settings		
Controller cycle time	T_s	$62.5\,\mu\mathrm{s}$
Controller hardware		dSPACE MicroLabBox
Processor		NXP QorIQ P5020, 2 cores, 2 GHz

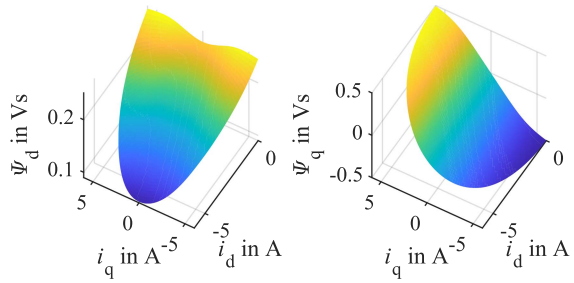

Fig. 11. Flux linkage maps of the considered test IPMSM.

TABLE II
Required Execution Times of the Proposed Scheme Implemented in C Running on a Lenovo T14 s With an AMD Ryzen 7 1.9-GHz Processor and 32 GB of RAM

	Execution time in microseconds
Motor model estimation (see Section III-A)	0.29
Rotor angle estimation (see Section III-B)	0.56
PLL (see Section III-C)	0.32
FCS-MPCC (see Section III-D)	0.72
Overall control scheme	1.89

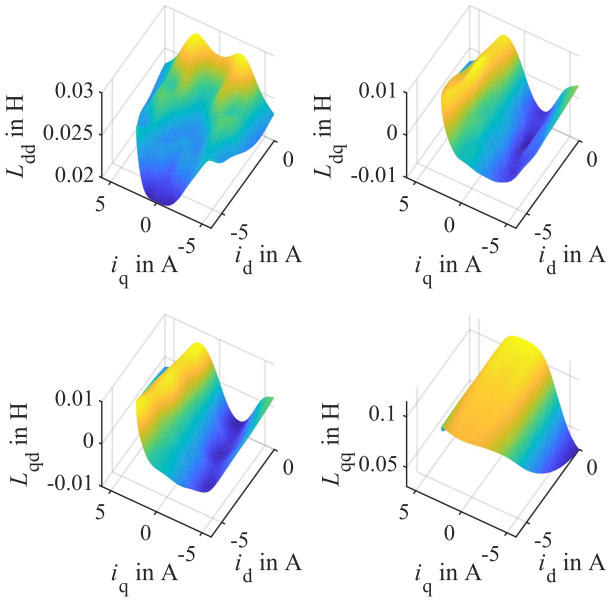

Fig. 12. Differential inductance maps of the considered test IPMSM.

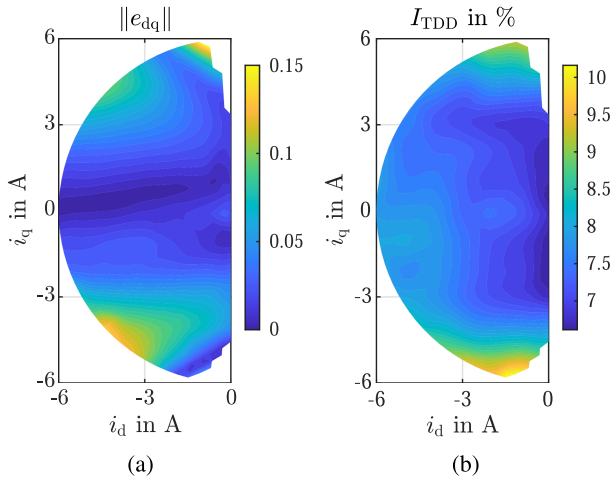

Fig. 13. Steady-state control performance investigation of the proposed method at $n_{me} = 750\,\mathrm{min}^{-1}$. (a) Steady-state control error. (b) Phase current distortion.

identification and rotor angle estimation is of similar magnitude than those of PLL and FCS-MPCC, the additional computational load compared to a sensored model-based FCS-MPCC can be considered as minor.

In order to prove the effectiveness and performance of the sensorless control, several representative experiments that were carried out are shown in the following.

B. Steady-State Investigation

Important performance criteria during steady-state operation for drive controllers are the current distortion that causes additional copper losses induced by the harmonic phase currents I_h, and the steady-state control error. Both metrics for the total demand distortion (TDD) [31]

$$I_{\mathrm{TDD}} = \frac{\sqrt{\sum_{h\neq 1} I_h^2}}{I_{\mathrm{nom}}} \tag{27}$$

as well as the norm of the normalized steady-state control error vector

$$\|\boldsymbol{e}_{\mathrm{dq}}\| = \frac{\|\boldsymbol{\mu}(\boldsymbol{i}_{\mathrm{dq}}) - \boldsymbol{i}^*_{\mathrm{dq}}\|}{I_{\mathrm{nom}}} \tag{28}$$

with the mean stator current $\boldsymbol{\mu}(\boldsymbol{i}_{\mathrm{dq}})$ are normalized with respect to the nominal current I_{nom}. The control error $\boldsymbol{e}_{\mathrm{dq}}$ is calculated with the mean current $\boldsymbol{\mu}(\boldsymbol{i}_{\mathrm{dq}})$ in the actual and not the estimated dq reference frame.

In order to compare the control performance in terms of TDD and control accuracy of the proposed method with a standard rotor angle-sensored FCS-MPCC as benchmark in steady-state operation, 80 equidistant operating points were recorded in the left i_{d}–i_{q} half-plane with a maximum length $\|\boldsymbol{i}_{\mathrm{dq}}\|$ of $6\,\mathrm{A} \approx \sqrt{2} I_{\mathrm{nom}}$. Each dataset of one operating point contains 32 000 samples, which corresponds to a measuring time of 2 s for different speeds of $n_{\mathrm{me}} = \{0; 30; 750; 1500\}\ \mathrm{min}^{-1}$.

The optimization problem of the benchmark FCS-MPCC is the same as for the proposed sensorless control, but without the additional inequality condition (24d) because neither the rotor angle nor the system matrices $\boldsymbol{B}_{\mathrm{dq}}$ and $\boldsymbol{E}_{\mathrm{dq}}$ must be identified. In contrast to the proposed method, the system matrices $\boldsymbol{B}_{\mathrm{dq}}$ and $\boldsymbol{E}_{\mathrm{dq}}$ are calculated with the help of the motor model (5) and LUTs of flux linkages and differential inductances; cf., Figs. 11 and 12.

Therefore, it is worth highlighting that the implemented benchmark FCS-MPCC represents an upper bound for the achievable performance of the proposed sensorless control scheme. Compared to the benchmark FCS-MPCC, the proposed sensorless control scheme does have access to the rotor angle measurement and motor model parameters, e.g., differential inductances and flux linkage LUTs. Consequently, the control performance of the proposed sensorless control method is decreased compared to the benchmark FCS-MPCC. In Fig. 13(b), the TDD of the phase current $I_{\mathrm{TDD}}(\boldsymbol{i}_{\mathrm{dq}})$ of the IPMSM controlled by the proposed method at a speed of $n_{\mathrm{me}} = 750\,\mathrm{min}^{-1}$ in the left i_{d}–i_{q} half plane is depicted. Here, an increased TDD can be observed for increased q-currents because of the strong saturation for high q-currents; cf., L_{qq} in Fig. 12.

The steady-state control error $\|\boldsymbol{e}_{\mathrm{dq}}(\boldsymbol{i}_{\mathrm{dq}})\|$ can be seen in Fig. 13(a). Reason for the significant steady-state control error is the angle estimation error shown in Fig. 14(a). This angle estimation error is mainly induced by the systematic angle estimation error caused by cross saturation; cf., Fig. 14(b). Since the information about the cross saturation cannot be identified with the sensorless scheme, a systematic angle estimation error, and therefore, a steady-state current control error is inevitable. However, the reference currents cover the complete left half plane, the resulting actual currents do not cover it since current operating points with increased q-current amplitudes are rotated to negative d-current because of cross saturation effects and the resulting angle estimation error; cf. Fig. 14.

TABLE III
PERFORMANCE COMPARISON OF THE PROPOSED SENSORLESS CONTROL SCHEME AND A BENCHMARK FCS-MPCC AT STEADY STATE IN THE ENTIRE LEFT i_d–i_q HALF PLANE

Method	Motor parameter-free	Sensorless	Inequality cond. (24d)	n_me in min^{-1}	$\overline{\|\boldsymbol{e}_\mathrm{dq}\|}$	$\overline{I_\mathrm{TDD}}$ in %	$\overline{\mu(\Delta\varepsilon)}$ in °	$\overline{\|\mu(\Delta\varepsilon)\|}$ in °
Benchmark FCS-MPCC	✗	✗	✗	0	0.015	-	-	-
				30	0.015	-	-	-
				750	0.009	4.07	-	-
				1500	0.009	4.27	-	-
Proposed sensorless control	✓	✓	✓	0	0.031	-	-0.9	1.4
				30	0.031	-	-0.3	1.3
				750	0.031	7.4	-0.1	1.3
				1500	0.036	6.91	0.0	1.4

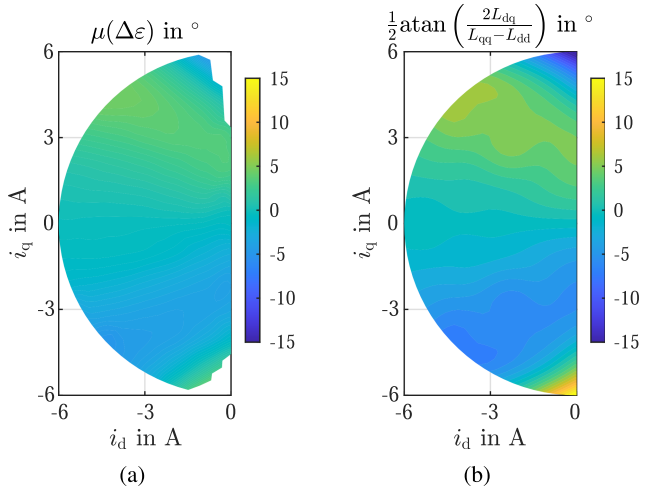

Fig. 14. Mean angle estimation error $\Delta\varepsilon$ and systematic estimation error due to cross saturation. (a) Mean angle estimation error $\Delta\varepsilon$ of the proposed method at $n_\mathrm{me} = 750\,\mathrm{min}^{-1}$. (b) Systematic estimation error calculated with (16) and the differential inductances; cf., Fig. 12.

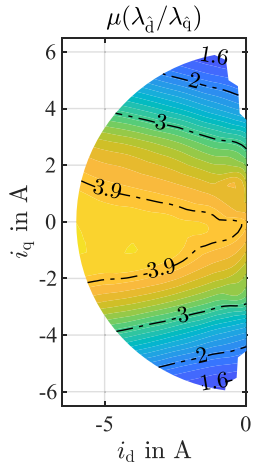

Fig. 15. Rotor saliency ratio of the test IPMSM identified by the proposed method at $n_\mathrm{me} = 750\,\mathrm{min}^{-1}$.

To obtain scalar values of the performance criteria of $x \in \{\|\boldsymbol{e}_\mathrm{dq}(\boldsymbol{i}_\mathrm{dq})\|, I_\mathrm{TDD}(\boldsymbol{i}_\mathrm{dq})\}$ for the proposed sensorless control and benchmark FCS-MPCC in the left i_d–i_q half plane, these are averaged over all 80 operating points

$$\overline{x} = \frac{1}{80}\sum_{l=1}^{80} x_l. \tag{29}$$

In addition, the performance criteria $\mu(\Delta\varepsilon)$ and $|\mu(\Delta\varepsilon)|$ are averaged for the proposed method, which corresponds to the mean error (ME) and the mean absolute error (MAE) of the angle estimation. Table III contains the resulting averaged performance criteria. For a speed of $n_\mathrm{me} = 30\,\mathrm{min}^{-1}$, the speed-controlled load motor is not able to ensure a constant speed because of a low rotor inertia and cogging torque. Therefore, the distortion of the phase currents $I_\mathrm{TDD}(\boldsymbol{i}_\mathrm{dq})$ is only evaluated for speeds of $n_\mathrm{me} = \{750; 1500\}\ \mathrm{min}^{-1}$. As a result of the inequality condition (24d) of the proposed method, the TDD is increased in comparison to the benchmark FCS-MPCC. The steady-state control error $\|\boldsymbol{e}_\mathrm{dq}(\boldsymbol{i}_\mathrm{dq})\|$ is greater for the proposed method, too. This is due to the systematic angle estimation error because of the cross-saturation effects.

The ME $\overline{\mu(\Delta\varepsilon)}$ for all speeds except standstill is close to zero. The reason for this increased ME at standstill are rotor-angle-dependent effects, e.g., slot harmonics. For all other speeds, rotor angle-dependent effects vanish by averaging per operating point. An ME $\overline{\mu(\Delta\varepsilon)}$ that is close to zero does not necessarily indicate mean angle estimation errors $\mu(\Delta\varepsilon)$ per operating point that are close to zero since positive and negative mean angle estimation errors $\mu(\Delta\varepsilon)$ are compensating each other; see Fig. 14(a). Therefore, the ME $\overline{\mu(\Delta\varepsilon)}$ can be only interpreted as constant bias of the angle estimation error that can be considered as negligible for the proposed sensorless control. In addition to the ME $\overline{\mu(\Delta\varepsilon)}$, the MAE $\overline{|\mu(\Delta\varepsilon)|}$ is provided as performance criterion that handles positive and negative angle estimation errors equivalently. Although significant cross-saturation exists at some locations in the left i_d–i_q half plane [high-magnitude q-currents, zero d-current; cf., Fig. 14(b)], and therefore, a locally increased angle estimation error occurs, the MAE $\overline{|\mu(\Delta\varepsilon)|}$ can be considered small for the test IPMSM. As additional functionality, the proposed scheme can be used to estimate the rotor saliency ratio, which corresponds to the ratio of the estimated eigenvalues $\lambda_{\hat{\mathrm{d}}}/\lambda_{\hat{\mathrm{q}}}$. The estimated mean saliency ratio $\mu(\lambda_{\hat{\mathrm{d}}}/\lambda_{\hat{\mathrm{q}}})$ in the left i_d-i_q half plane is shown in Fig. 15. Here, the saliency ratio decreases from approx. 4 to approx. 1.6 due to heavy saturation in the q-axis of the test IPMSM.

C. Transient Current Investigation

To investigate the angle estimation and control performance of the proposed scheme during current transients, an operating point change from the origin to a guess of the rated operation

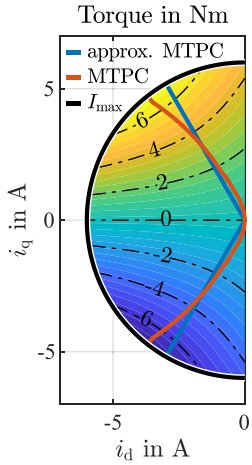

Fig. 16. Actual and approx. MTPC loci of the test IPMSM.

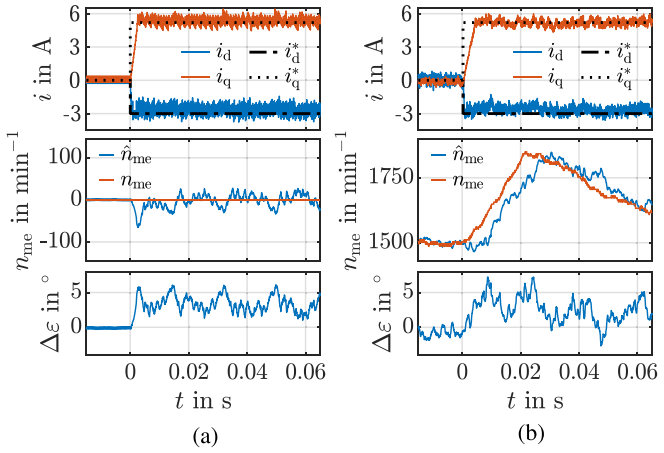

Fig. 17. Current step response to the rated operating point $\boldsymbol{i}_{dq}^* = [-3 \quad 5.2]^\top$ A at standstill and 50% rated speed. (a) $n_{me} = 0\,\text{min}^{-1}$(clamped rotor). (b) $n_{me} = 1500\,\text{min}^{-1}$.

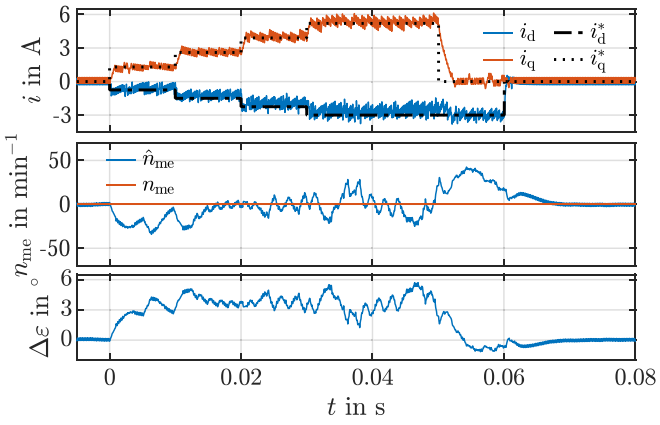

Fig. 18. Sequence of current step responses at $n_{me} = 0\,\text{min}^{-1}$ with a clamped rotor.

point (intersection between the maximum torque per current (MTPC) locus and the maximum current I_{max}) is performed. Since the MTPC locus is not known a priori, it must be approximated for control schemes without motor parameter knowledge to compute the rated operating point. As an initial guess, straight lines with an angle of 30 ° to the q-axis are chosen as an a priori MTPC locus (cf., Fig. 16), which results in a rated operating point of $\boldsymbol{i}_{dq}^* = [-3 \quad 5.2]^\top$ A.

In Fig. 17, the current transients and angle as well as speed estimations of the proposed scheme from $\boldsymbol{i}_{dq}^* = \boldsymbol{0}$ A to the rated operating point for standstill operation (clamped rotor) and $n_{me} = 1500\,\text{min}^{-1}$ can be seen. Additionally, in Fig. 18, a sequence of current step responses at standstill with clamped rotor are shown. In both figures, fast current control performance can be observed due to the high control dynamic of the applied FCS-MPCC. The angle estimation error resulting from cross saturation leads to minor steady-state control. A reason for the increased variance of the angle, and therefore, also of the speed estimation at the rated operating point compared to the origin could be the decreased saliency ratio at the rated operating point of approx. 1.6 compared to the saliency ratio of approx. 3.9 at the origin; cf., Fig. 15. For a decreasing rotor saliency, the sensitivity of the angle estimation to parasitic effects, e.g., measurement noise or nonsinusoidal flux linkage distribution in the air gap due to the winding scheme or other harmonic effects is increased, which increases the variance of the angle estimate.

D. Transient Speed Investigation

Since the applied PLL contains two integrators, a zero steady-state observation error of the angle can only be achieved by the PLL for constant speeds. Therefore, a transient observation error during speed transients occurs. The magnitude of this estimated angle error depends on the speed dynamics and the choice of the characteristic frequency of the PLL. In particular, a high-speed dynamic combined with a small characteristic frequency results in a large estimation error; cf. (21). In Fig. 19, a speed transient from $-n_{me,nom}/2 = -1500\,\text{min}^{-1}$ to $n_{me,nom}/2 = 1500\,\text{min}^{-1}$ is conducted by the speed-controlled load machine during rated operation $\boldsymbol{i}_{dq}^* = [-3 \quad 5.2]^\intercal$ A of the IPMSM in approx. 100 ms. This dynamic speed change corresponds to an acceleration of $30000\,\text{min}^{-1}/\text{s}$. During the speed transient, an angle estimation error $\Delta\varepsilon$ of up to 15 ° results. Because of the angle estimation error during the speed ramp, an increased current control error occurs. The angle estimation error induced by the PLL calculated using (21) for this scenario with a slope of the speed ramp of $30000\,\text{min}^{-1}/\text{s}$ and the PLL tuning parameters ($D = 1$, $\omega_0 = 2\pi \cdot 50\,\text{Hz}$) corresponds to $\Delta\varepsilon_{PLL} \approx 3.6\,°$. This seems to be inline with the increased mean of the angle estimation error during the speed ramp compared to constant speed operation ($t < 0$); see Fig. 19.

It is worth to note that the increase of the angle estimation error during speed transients due to the limited bandwidth of the PLL occurs for all other PLL-based rotor angle sensorless schemes in the same way. Even for schemes with measured rotor angles that utilize a PLL to observe the speed and smoothen the angle measurement, e.g., due to the application of a low-cost angle sensor, the same increase in the angle estimation error occurs.

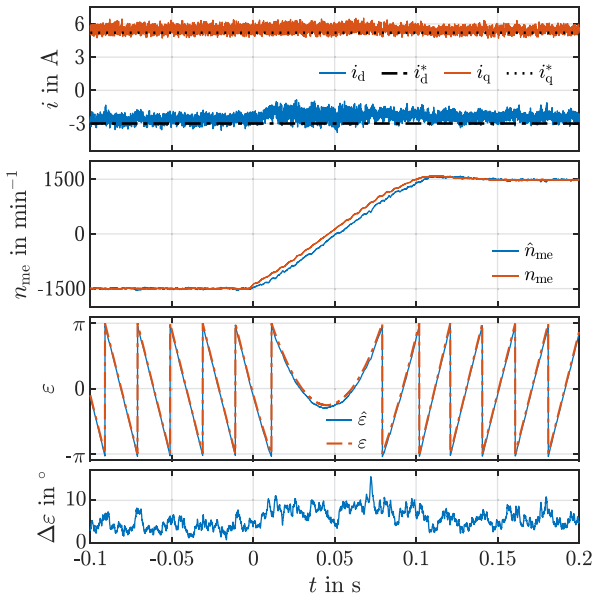

Fig. 19. Speed change from $-n_{\mathrm{me,nom}}/2 = -1500\,\mathrm{min}^{-1}$ to $n_{\mathrm{me,nom}}/2 = 1500\,\mathrm{min}^{-1}$ conducted by the load machine during rated operation at $\boldsymbol{i}_{\mathrm{dq}}^* = [-3 \quad 5.2]^\top$ A in approx. 100 ms.

V. Conclusion

In this article, a rotor anisotropy-based sensorless control scheme with minimum a priori motor knowledge and tuning effort for the current control of IPMSMs for slow to medium speeds including standstill was presented and experimentally investigated. The motor model is identified with the help of an additional excitation inequality constraint in the cost function of the applied FCS-MPCC. The disadvantages and advantages of this method can be summarized as follows.

Disadvantages:

1) Current distortion is increased compared to FCS-MPCC with full motor parameters knowledge and with measured rotor angle due to the additional excitation.
2) Average maximum applicable voltages are decreased by a factor of $1/3$ compared to model-based FCS-MPCC with measured rotor angle due to the additional excitation.
3) Systematic angle estimation errors due to cross-saturation effects occur.

Advantages:

1) A priori motor parameter knowledge is not required.
2) No parameters must be tuned, except for special applications with highly dynamic speed transients. Here, an automatic tuning procedure for the characteristic frequency of the PLL is proposed.
3) Highly dynamic step-like current and speed transients can be handled.

These advantages allow rotor angle-sensorless control of IPMSM drives without any prior human work contribution, which is especially interesting for automated IPMSM drive commissioning procedures and low-cost applications.

In the future, the required additional excitation that increases harmonic current distortion and reduces the maximum available mean voltage should be decreased. This could be achieved by applying inverter switching schemes with lower harmonic content, e.g., discrete space vector modulation. Furthermore, it should be investigated whether physical motor parameters (differential inductances and flux linkages) can be extracted from the identified motor model to store them in LUTs as proposed in [32] for a rotor angle sensored scheme, enabling the selection of loss-optimal reference currents for a given torque reference with the help of a higher level open-loop torque controller [33].

References

[1] S. Sul and S. Kim, "Sensorless control of ipmsm: Past, present, and future," *IEEJ J. Ind. Appl.*, vol. 1, no. 1, pp. 15–23, 2012.
[2] G. Wang, M. Valla, and J. Solsona, "Position sensorless permanent magnet synchronous machine drives—a review," *IEEE Trans. Ind. Electron.*, vol. 67, no. 7, pp. 5830–5842, Jul. 2020.
[3] Z. Chen, M. Tomita, S. Doki, and S. Okuma, "An extended electromotive force model for sensorless control of interior permanent-magnet synchronous motors," *IEEE Trans. Ind. Electron.*, vol. 50, no. 2, pp. 288–295, Apr. 2003.
[4] I. Boldea, M. Paicu, and G. Andreescu, "Active flux concept for motion-sensorless unified AC drives," *IEEE Trans. Power Electron.*, vol. 23, no. 5, pp. 2612–2618, Sep. 2008.
[5] G. Wang, T. Li, G. Zhang, X. Gui, and D. Xu, "Position estimation error reduction using recursive-least-square adaptive filter for model-based sensorless interior permanent-magnet synchronous motor drives," *IEEE Trans. Ind. Electron.*, vol. 61, no. 9, pp. 5115–5125, Sep. 2014.
[6] Y. Zhao, Z. Zhang, W. Qiao, and L. Wu, "An extended flux model-based rotor position estimator for sensorless control of salient-pole permanent-magnet synchronous machines," *IEEE Trans. Power Electron.*, vol. 30, no. 8, pp. 4412–4422, Aug. 2015.
[7] R. Dhaouadi, N. Mohan, and L. Norum, "Design and implementation of an extended kalman filter for the state estimation of a permanent magnet synchronous motor," *IEEE Trans. Power Electron.*, vol. 6, no. 3, pp. 491–497, Jul. 1991.
[8] Z. Guchuan, A. Kaddouri, L. A. Dessaint, and O. Akhrif, "A nonlinear state observer for the sensorless control of a permanent-magnet AC machine," *IEEE Trans. Ind. Electron.*, vol. 48, no. 6, pp. 1098–1108, Dec. 2001.
[9] Z. Qiao, T. Shi, Y. Wang, Y. Yan, C. Xia, and X. He, "New sliding-mode observer for position sensorless control of permanent-magnet synchronous motor," *IEEE Trans. Ind. Electron.*, vol. 60, no. 2, pp. 710–719, Feb. 2013.
[10] J.-H. Jang, S.-K. Sul, J.-I. Ha, K. Ide, and M. Sawamura, "Sensorless drive of surface-mounted permanent-magnet motor by high-frequency signal injection based on magnetic saliency," *IEEE Trans. Ind. Appl.*, vol. 39, no. 4, pp. 1031–1039, Jul./Aug. 2003.
[11] H.-S. Kim and K. Lee, "Model predictive current control with online parameter estimation for synchronous reluctance machine controlled by high-frequency signal injection position-sensorless," in *IEEE Access*, vol. 10, pp. 25267–25277, 2022.
[12] M. J. Corley and R. D. Lorenz, "Rotor position and velocity estimation for a salient-pole permanent magnet synchronous machine at standstill and high speeds," *IEEE Trans. Ind. Appl.*, vol. 34, no. 4, pp. 784–789, Jul./Aug. 1998.
[13] L. Ortombina, M. Berto, and L. Alberti, "Sensorless drive for salient synchronous motors based on direct fitting of elliptical-shape high-frequency currents," *IEEE Trans. Ind. Electron.*, vol. 70, no. 4, pp. 3394–3403, Apr. 2023.
[14] E. Robeischl and M. Schroedl, "Optimized INFORM measurement sequence for sensorless PM synchronous motor drives with respect to minimum current distortion," in *Proc. IEEE 37th Annu. Meeting Ind. Appl. Soc.*, 2002, pp. 92–98.
[15] M. Schroedl, "Sensorless control of AC machines at low speed and standstill based on the "INFORM" method," in *Proc. IEEE 31st Annu. Meeting Ind. Appl. Soc.*, 1996, pp. 270–277.

[16] A. Varatharajan, P. Pescetto, and G. Pellegrino, "Injectionless sensorless control of synchronous reluctance machine for zero to low speeds region," in *Proc. IEEE 9th Int. Symp. Sensorless Control Elect. Drives*, 2018, pp. 72–77.
[17] P. G. Carlet, F. Tinazzi, L. Ortombina, and N. Bianchi, "Sensorless motor parameter-free predictive current control of synchronous reluctance motor drives," in *Proc. Int. Conf. Elect. Mach.*, 2022, pp. 1464–1470.
[18] Y. Hua, G. M. Asher, M. Sumner, and Q. Gao, "Sensorless control of surface mounted permanent magnetic machine using the standard space vector PWM," in *Proc. IEEE Annu. Meeting Ind. Appl. Soc.*, 2007, pp. 661–667.
[19] Q. Gao, G. M. Asher, M. Sumner, and L. Empringham, "Position estimation of a matrix-converter-fed AC PM machine from zero to high speed using PWM excitation," *IEEE Trans. Ind. Electron.*, vol. 56, no. 6, pp. 2030–2038, Jun. 2009.
[20] A. Piippo, M. Hinkkanen, and J. Luomi, "Adaptation of motor parameters in sensorless PMSM drives," *IEEE Trans. Ind. Appl.*, vol. 45, no. 1, pp. 203–212, Jan./Feb. 2009.
[21] S. Ichikawa, M. Tomita, S. Doki, and S. Okuma, "Sensorless control of permanent-magnet synchronous motors using online parameter identification based on system identification theory," *IEEE Trans. Ind. Electron.*, vol. 53, no. 2, pp. 363–372, Apr. 2006.
[22] W. Peters and J. Böcker, "Discrete-time design of adaptive current controller for interior permanent magnet synchronous motors (IPMSM) with high magnetic saturation," in *Proc. IEEE 39th Annu. Conf. Ind. Electron. Soc.*, 2013, pp. 6608–6613.
[23] A. Specht, S. Ober-Blöbaum, O. Wallscheid, C. Romaus, and J. Böcker, "Discrete-time model of an IPMSM based on variational integrators," in *Proc. IEEE Int. Electric Mach. Drives Conf.*, 2013, pp. 1411–1417.
[24] J. Böcker, "Discrete-time model of an induction motor," *Eur. Trans. Elect. Power*, vol. 1, no. 2, pp. 65–71, 1991.
[25] S. Kühl, P. Landsmann, and R. M. Kennel, "Compensating angle estimation errors caused by magnetic saturation in anisotropy-based sensorless control schemes," in *Proc. IEEE 3rd Int. Symp. Sensorless Control Elect. Drives*, pp. 1–6. 2012.
[26] N. Bianchi, S. Bolognani, J. Jang, and S. Sul, "Comparison of PM motor structures and sensorless control techniques for zero-speed rotor position detection," *IEEE Trans. Power Electron.*, vol. 22, no. 6, pp. 2466–2475, Nov. 2007.
[27] J. Holtz, "Acquisition of position error and magnet polarity for sensorless control of PM synchronous machines," *IEEE Trans. Ind. Appl.*, vol. 44, no. 4, pp. 1172–1180, Aug. 2008.
[28] P. Cortes, J. Rodriguez, C. Silva, and A. Flores, "Delay compensation in model predictive current control of a three-phase inverter," *IEEE Trans. Ind. Electron.*, vol. 59, no. 2, pp. 1323–1325, Feb. 2012.
[29] A. Brosch, S. Hanke, O. Wallscheid, and J. Böcker, "Data-driven recursive least squares estimation for model predictive current control of permanent magnet synchronous motors," *IEEE Trans. Power Electron.*, vol. 36, no. 2, pp. 2179–2190, Feb. 2021.
[30] L. Ortombina, F. Tinazzi, and M. Zigliotto, "Magnetic modeling of synchronous reluctance and internal permanent magnet motors using radial basis function networks," *IEEE Trans. Ind. Electron.*, vol. 65, no. 2, pp. 1140–1148, Feb. 2018.
[31] T. Geyer, "Model predictive direct current control: Formulation of the stator current bounds and the concept of the switching horizon," *IEEE Ind. Appl. Mag.*, vol. 18, no. 2, pp. 47–59, Mar./Apr. 2012.
[32] A. Brosch, O. Wallscheid, and J. Böcker, "Long-term memory recursive least squares online identification of highly utilized permanent magnet synchronous motors for finite-control-set model predictive control," *IEEE Trans. Power Electron.*, vol. 38, no. 2, pp. 1451–1467, Feb. 2023.
[33] H. Eldeeb, C. M. Hackl, L. Horlbeck, and J. Kullick, "A unified theory for optimal feedforward torque control of anisotropic synchronous machines," *Int. J. Control*, vol. 91, no. 10, pp. 2273–2302, 2018.

Anian Brosch received the bachelor's and master's degrees in mechanical engineering from the Munich University of Applied Sciences, Munich, Germany, in 2016 and 2018, respectively.

Since 2018, he has been working as a Research Associate with the Department of Power Electronics and Electrical Drives, Paderborn University, Paderborn, Germany. His research interests include identification and control of electrical drives, in particular model predictive control of highly utilized permanent-magnet synchronous motors.

Fabio Tinazzi (Member, IEEE) received the B.S., M.S., and Ph.D. degrees in mechatronic engineering from the University of Padova, Vicenza, Italy, in 2008, 2011, and 2016, respectively.

From July 2023, he is an Associate Professor with the Department of Management and Engineering, University of Padova. His main research interests include sensorless control, predictive control, and parameter estimation techniques for ac motors.

Dr. Tinazzi is the President of the IEEE Industry Applications Society, Industrial Electronics Society, and Power Electronics Society (IEEE IAS-IES-PELS) North Italy Joint Chapter.

Oliver Wallscheid (Senior Member, IEEE) received the bachelor's (Hons.) and master's (Hons.) degrees in industrial engineering, and the doctorate (Hons.) degree in electrical engineering from the Paderborn University, Paderborn, Germany, in 2010, 2012, and 2017, respectively.

Since 2017, he has been a Senior Research Fellow with the Department of Power Electronics and Electrical Drives, Paderborn University. His research interests include data-driven identification and intelligent control of electrical power systems in decentralized grids, power electronics, and drives.

Mauro Zigliotto (Senior Member, IEEE) received the master's (Hons.) degree in electronic engineering from the University of Padova, Padova, Italy, in 1988.

From 1989 to 1992, he was the Head of the R&D Office, ITACO. In 1992, he joined the University of Padova as an Assistant Professor and in 2000, he joined the University of Udine, Udine, Italy, where he became an Associate Professor. He is currently a Full Professor of electrical machines and drives with the University of Padova and is also the Head of the Electric Drives Laboratory, Vicenza, Italy. His research interests include advanced control strategies and self-commissioning for ac motors and AI-based techniques for early fault monitoring in ac drives.

Joachim Böcker (Senior Member, IEEE) received the Dipl.-Ing. and Dr.-Ing. degrees in electrical engineering from the Berlin University of Technology, Berlin, Germany, in 1982 and 1988, respectively.

From 1988 to 2001, he was with AEG and Daimler Research as the Head of the Control Engineering Team of the Electrical Drive Systems Laboratory. In 2001, he started his own business in the area of control engineering, electrical drives, and power electronics. In 2003, he joined Paderborn University, Germany, as a Full Professor and the Head of the Department of Power Electronics and Electrical Drives. In 2023, he retired from the position. The research interests of his group include electrical drives, particularly for electric vehicles (EVs) and hybrid electric vehicles, energy management strategies for vehicles and smart grids, and converters for power supplies, EV chargers, and renewables.